



One-step in-situ preparation of N-doped TiO₂@C derived from Ti₃C₂ MXene for enhanced visible-light driven photodegradation

Huoshuai Huang^a, Yun Song^{a,b}, Najun Li^{a,b,*}, Dongyun Chen^{a,b}, Qingfeng Xu^{a,b}, Hua Li^{a,b}, Jinghui He^{a,b}, Jianmei Lu^{a,b,*}

^a College of Chemistry, Chemical Engineering and Materials Science, Collaborative Innovation Center of Suzhou Nano Science and Technology, Soochow University, Suzhou, Jiangsu 215123, China

^b National Center of International Research on Intelligent New Nanomaterials and Detection Technologies in Environmental Protection, Suzhou, Jiangsu 215123, China



ARTICLE INFO

Keywords:
Ti₃C₂ MXene
Nitrogen doping
TiO₂@C
In-situ preparation
Photocatalysis

ABSTRACT

As the most promising environment-friendly photocatalyst, titanium dioxide admittedly has two shortcomings of low sunlight utilization efficiency and poor quantum yield. Nitrogen doping and TiO₂ loading on carbon materials can improve the above two problems, respectively. But a facile synthetic method for titanium dioxide composites with stable structure and high visible-light-driven photocatalytic activity is still desired by researchers. Herein we obtained two-dimensional layered nitrogen-doped carbon-supported titanium dioxides (N-TiO₂@C) via a one-step in-situ fabrication way from a novel two-dimensional layered transition metal carbide Ti₃C₂ MXene as carbon skeleton and homologous titanium source. Based on the negatively charged and easily oxidized property of Ti₃C₂ MXene, it was assembled with nitrogen-containing cationic compound via electrostatic interactions and then in-situ transformed into nitrogen-doped carbon-supported TiO₂ in a CO₂ atmosphere at 550 °C. The obtained composites of porous 2D layered N-TiO₂@C with high stability, outstanding electron transfer performance and excellent visible-light photocatalytic activity exhibits the high efficiency of phenol degradation with the apparent rate constant k of $1.646 \times 10^{-2} \text{ min}^{-1}$. It provides a facile new method for the preparation of visible-light-driven titanium dioxide with excellent catalytic performance, structural stability and good application prospects in the environmental purification.

1. Introduction

Nowadays, the utilization of solar energy and the treatment of environmental pollution are important issues for humanity. How to use the power of the solar energy to solve the problem of environmental pollution has become a focus of attention. Photocatalysis, as a new technology for pollution control with mild conditions, low energy consumption and friendly environment, is based on the photocatalytic materials [1]. In the past decades, titanium dioxide (TiO₂) is widely studied and used as a promising and environmental-friendly photocatalyst owing to its strong oxidizing power, nontoxicity, high chemical stability and photostability [2]. However, the anatase type TiO₂ has a band gap of about 3.2 eV and it only absorbs 5% of the sunlight in UV region. In addition, its photogenerated electrons and holes are likely to recombine, resulting in low utilization of photogenerated carriers. Therefore, how to effectively improve the utilizing ratio of sunlight and the optical quantum efficiency of TiO₂ is a key scientific issue for

driving its large-scale application in the environment and energy field.

To solve the problems of wide band gap and low visible light utilization of TiO₂, researchers have expanded the response range of titanium dioxide into visible light region by means of element doping, precious metal deposition, semiconductor composite, dye sensitization and preparation of TiO₂ with special morphology, so as to improve photocatalytic activity [3–10]. Among them, improving the visible-light photocatalytic activity of titanium dioxide by nitrogen doping is commonly used [11,12]. In order to solve the problem of easy recombination of photoelectrons and holes in titanium dioxide, a common modification method of TiO₂ is to load nano-carbon-based materials with excellent conductivity and large specific surface area to form C/TiO₂ composites [13–15]. However, there are many problems in composite materials, such as weak loading, uneven dispersion and easy agglomeration of titanium dioxide on the surface of carbon materials. It is important to find a new method for the preparation of C/TiO₂ composite materials with stable structure, large specific surface area and

* Corresponding authors at: College of Chemistry, Chemical Engineering and Materials Science, Collaborative Innovation Center of Suzhou Nano Science and Technology, Soochow University, Suzhou, Jiangsu 215123, China.

E-mail addresses: linajun@suda.edu.cn (N. Li), lujm@suda.edu.cn (J. Lu).

excellent photocatalytic performance.

MXene, a new class of two-dimensional transition metal carbides or nitrides, has attracted more and more attention since the first report of Ti_3C_2 by Yury Gogotsi's team in 2011 [16]. The general formula of MXene is $M_{n+1}X_n$ ($n = 1, 2, 3$), where M represents an early transition metal and X stands for carbon and/or nitrogen element. These 2D MXenes have been synthesized via selective etching the "A" layer from their corresponding layer-structured MAX by hydrofluoric acid (HF), which "A" refer to Al or Si element. MXene's unique two-dimensional morphology, chemical composition and surface chemical functional groups (e.g., $-OH$, $-O$ and $-F$) endow it with good metal conductivity, negatively charged surface, hydrophilicity, bending stiffness superior to graphene and other special properties, and its properties can be regulated by changes in element composition and surface functional groups [17]. Therefore, MXene has shown good application prospects in many fields, such as electrochemical energy storage materials, sensors, catalysts in chemical industry, conductive reinforcement phase of polymers, environmental management, etc [18–21].

It is noteworthy that MXene is unstable in air (oxygen) atmosphere and high temperature conditions due to the exposure of high proportion of metal atoms on the surface. Previous studies have shown that Ti_3C_2 MXene can be partially transformed into TiO_2 by long-term preservation in water without oxygen removal or heating above 200 °C in an oxidizing atmosphere, accompanied by the crystalline phase transition process of TiO_2 [22–26]. Rapid oxidation at high temperature is conducive to the transformation of Ti_3C_2 to anatase [27]. Two-dimensional layered composites C/ TiO_2 can be prepared by rapidly heating up to 700 °C in CO_2 atmosphere [28]. The thermal stability of Mxene material limits the application of MXene, but at the same time, we are surprised to find that the one-step in-situ synthesis of C/ TiO_2 can be achieved based on the characteristics of Ti_3C_2 MXene which is easy to oxidize to C/ TiO_2 under oxidizing atmosphere and high temperature [29].

Herein, the novel two-dimensional layered transition metal carbide Ti_3C_2 MXene serves as carbon skeleton and titanium source. Based on the negatively charged and easily oxidized properties of Ti_3C_2 MXene itself, the nitrogen-containing cationic compound can be assembled on the negatively charged surface of ultrathin Ti_3C_2 MXene via electrostatic interactions. And then in-situ transformation of Ti_3C_2 into N-doped carbon-supported TiO_2 is performed by controlling the oxidation conditions (Scheme 1). The obtained composites of porous 2D layered N- $TiO_2@C$ with stable structure, good conductivity and enhanced visible-light photocatalytic activity have good application prospects in wastewater treatment and air purification.

2. Experimental section

2.1. Materials

Hydrochloric acid (37%), tetrabutyl titanate and absolute ethyl alcohol were purchased from TCI; Lithium fluoride (LiF) and melamine were obtained from Alfa Aesar; Cetyltrimethyl ammonium bromide (CTAB) was bought from Sigma-Aldrich; Ti_3AlC_2 was provided by Nanjing Mission New Materials Co., Ltd. All chemicals were used without further treatment.

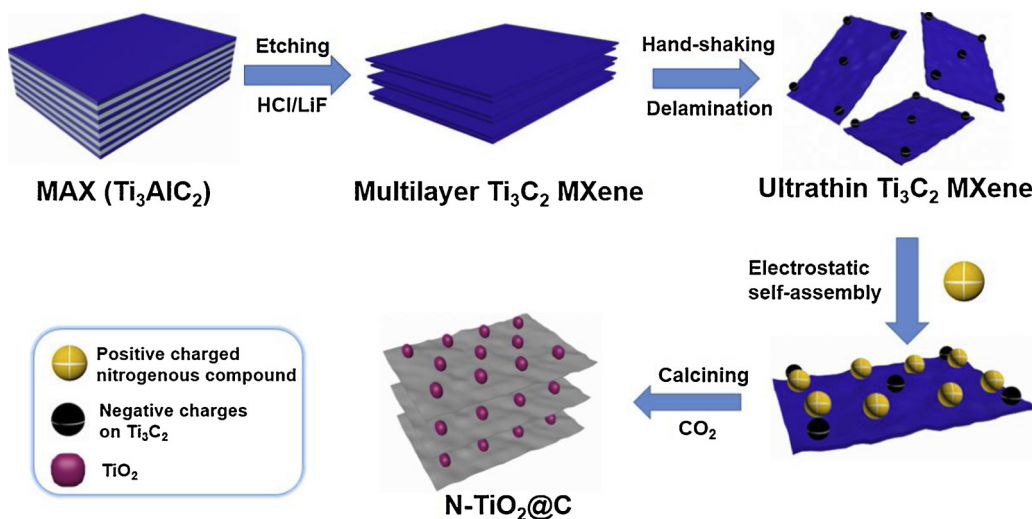
2.2. Characterization

Scanning electron microscopy (SEM, Hitachi SU8010) were served to analyze the morphology of all the samples. The transmission electron microscopy (TEM) images, high-resolution TEM (HRTEM) images and elemental mapping were observed with Hitachi H600. X-Ray powder diffraction (XRD) patterns were recorded with X' Pert-Pro MPD with Cu $K\alpha$ radiation. X-ray photoelectron spectroscopy (XPS) was measured by ESCALAB MK II with Al- $K\alpha$ radiation. Ultraviolet-visible (UV-vis) spectra were measured by Shimadzu UV-3600. The photoluminescence (PL) emission spectra were obtained from a FLS920 fluorescence spectrophotometer. The concentration of phenol was analyzed by high-performance liquid chromatography (HPLC, Agilent 1260). Electron spin-resonance spectroscopy (ESR, JEOL JES-X320) was used to detect radicals spin-trapped by 5,5'-dimethyl-1-pyrroline-N-oxide (DMPO) of which center field (336 mT), microwave frequency (9.15 GHz) and power (1 mW) are set. Zeta potential was measured by a Malvern Zetasizer Nano ZS (Malvern Instruments).

2.3. Fabrication of photocatalyst N- $TiO_2@C$

2.3.1. Synthesis of the ultrathin Ti_3C_2 MXene

0.8 g of LiF was added to 10 mL of 9 M HCl and stirred for 5 min, then 0.5 g of Ti_3AlC_2 was added to the mixed solution over another 5 min to avoid violent reaction, the mixed solution was reacted for 24 h by stirring at room temperature. The reaction product was washed several times via centrifugation (5 min per cycle at 3500 rpm) to acquire multilayer Ti_3C_2 MXene (*m*- Ti_3C_2 MXene) until the pH of the suspension is about 5~6, redisperse with 50 ml of water and shaked for 15 min to obtain a clay-like, large-sized ultrathin Ti_3C_2 MXene (*u*- Ti_3C_2 MXene) black colloidal solution (*u*- Ti_3C_2 MXene content \approx 0.5 mg/mL).



Scheme 1. The schematic illustration for the preparation of 2D layered N- $TiO_2@C$.

2.3.2. Synthesis of N-TiO₂@C heterojunctions

The 50 mL of *u*-Ti₃C₂ MXene colloidal suspension with 100 mg of nitrogen-containing cationic compound (positively charged melamine or CTAB) dissolved in 50 mL of 0.1 M dilute hydrochloric acid have a mass ratio of 1:4 according to the *u*-Ti₃C₂ MXene and nitrogen-containing cationic compound. Sediments were collected by centrifugation and freeze-drying. Subsequently, it was calcined under CO₂ atmosphere at a heating rate of 6 °C / min to 550 °C with CO₂ flow rate of 75 sccm for 4 h, and then naturally cooled to get the final product. The final products of electrostatic self-assembly with positively charged melamine and CTAB were named as N-TiO₂@C-CHN and N-TiO₂@C-CTAB, respectively. Preparation of the controlled C/TiO₂ from tetrabutyl titanate and glucose by hydrothermal method and the positively charged melamine are shown in SI.

2.4. Photocatalytic activity test

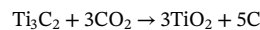
50 mg of photocatalyst was added to 50 mL of 20 ppm phenol solution and stirred for 1 h in the dark to achieve adsorption-desorption equilibrium. Then, the reaction was carried out under the irradiation of a xenon lamp (with a light filter > 420 nm), and 1 mL of a suspension was taken centrifuged at regular intervals to analyze the concentration of phenol. The concentration of phenol was determined by high performance liquid chromatography (HPLC). The mobile phase was methanol and water (volume ratio: 60/40), the flow rate was 1 ml/min, and the Detection wavelength was 270 nm [30].

3. Results and discussion

Scheme 1 simply illustrated the preparation of 2D layered N-TiO₂@C. Firstly, Ti₃AlC₂ MAX was etched by LiF/HCl to obtain *m*-Ti₃C₂ MXene, and then *u*-Ti₃C₂ MXene was obtained by hand-shaking. Subsequently, the *u*-Ti₃C₂ MXene was electrostatically self-assembled with nitrogen-containing cationic compound, freeze-dried and calcined in a CO₂ atmosphere. After naturally cooling, two-dimensional nitrogen-doped carbon-supported titanium dioxides (2D layered N-TiO₂@C) was obtained.

The results of X-ray diffraction (XRD) pattern analysis were shown in **Fig. 1a**. Comparing Ti₃AlC₂ MAX with Ti₃C₂ MXene, the disappearance of the diffraction peaks around 39° can be observed in the XRD pattern, which shows that the Al layer is successfully removed by etching. And the (002) plane is shifted from 9.7° to a lower angle of 6.7°, indicates an increase of *d*-spacing of (002) and successful synthesis of Ti₃C₂ MXene. After calcination, the characteristic diffraction peaks of Ti₃C₂ MXene disappeared completely. The patterns of N-TiO₂@C-CHN, N-TiO₂@C-CTAB and C/TiO₂ all show the characteristic diffraction peaks of anatase TiO₂ (JCPDS no.21-1272) at 25.28, 37.8, 48.05, 53.89, 55.06, and 62.69°, indicating that Ti₃C₂ has been oxidized into TiO₂ by

the following reaction equation:



Among them, rutile phase characteristic peaks (JCPDS No. 21-1276) also appear in N-TiO₂@C-CHN, which is weaker than the peak intensity of anatase, indicating that only a small part of crystal transformation has taken place. This may be related to the higher nitrogen content of N-TiO₂@C-CHN, because melamine nitrogen content is higher than CTAB of the same mass. XRD did not detect carbon matrix due to its disordered structure or low content. To further confirm their structure, Raman spectroscopy (**Fig. 1b**) was performed to identify the presence of carbon. N-TiO₂@C-CHN, N-TiO₂@C-CTAB and C/TiO₂ all display characteristic peaks of the anatase at 156, 396, 510, 640 cm⁻¹ of E_g, B_{1g}, A_{1g} + B_{1g}, and the E_g modes, respectively. In addition, the Raman patterns displayed two carbon-related peaks, the disordered (D band) peak of 1340 cm⁻¹ and graphitic (G band) structures peak of 1590 cm⁻¹ revealed the presence of carbon layer in N-TiO₂@C and C/TiO₂. The G band is connected with the in-plane vibration of sp² carbon atoms and the D band is related to defects [31]. The I_D/I_G ratio is greater than 1, which indicates a higher proportion of defects in carbon layer.

Fig. 2a showed a scanning electron microscope (SEM) image of Ti₃AlC₂ and **Fig. 2b** represents a typical accordion-like multilayer Ti₃C₂ MXene, indicating that the Al layer was successfully etched. After hand-shaking and centrifugation, the multilayer Ti₃C₂ MXene was separated into ultrathin Ti₃C₂ MXene (**Fig. 2c**). Compared with literature [17], the LiF/HCl etching method is milder than the HF etching method and the obtained nanosheets have large size and few surface defects. It is noteworthy that when the nanosheets overlap with each other, the shape of the underlying nanosheets can still be clearly identified, indicating that they are ultrathin nanosheets. **Fig. 2d** showed a SEM diagram of electrostatic self-assembly of *u*-Ti₃C₂ MXene with nitrogen-containing cationic compound (positively charged melamine and CTAB were investigated here). In order to prove the practicability of electrostatic assembly, the zeta potential values of positively charged melamine, CTAB and Ti₃C₂ MXene were measured to be + 14.7 mV, + 58.1 mV and -50.4 mV, respectively, as shown in Table S1. The electrostatic self-assembly process was shown in **Fig. 2(g)**. The Ti₃C₂ MXenes colloidal suspension was very stable owing to its hydrophilicity and the electrostatic repulsion between adjacent nanolayers. When the nitrogen-containing cationic compounds were added, they were electrostatically adsorbed on the negative charged surface of *u*-Ti₃C₂ MXene, and the colloid was coalesced and a clarified supernatant was observed. It is noteworthy that the insertion of nitrogen-containing cationic compounds after self-assembly can effectively reduce the stacking of *u*-MXene and become wrinkled. After oxidation treatment at high temperature, **Fig. 2(e-f)** revealed the calcined product, N-TiO₂@C. It could be clearly seen that the N-TiO₂@C still maintains a two-dimensional

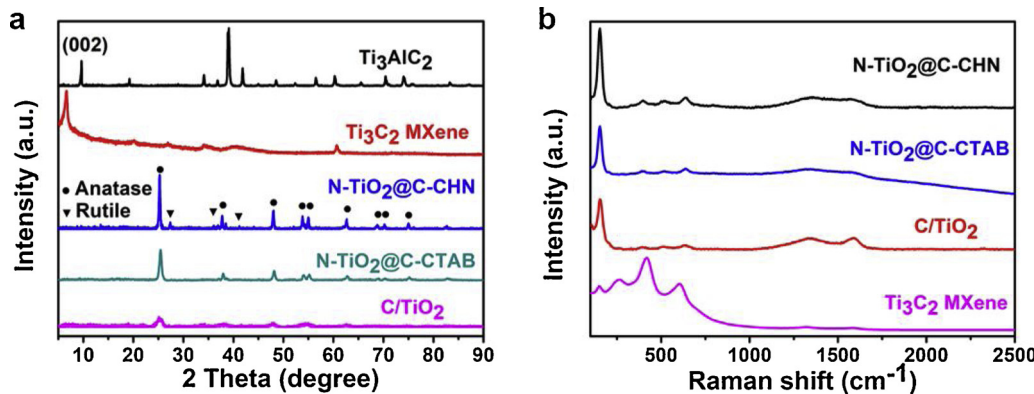


Fig. 1. (a) The XRD patterns of Ti₃AlC₂, Ti₃C₂ MXene, N-TiO₂@C-CHN, N-TiO₂@C-CTAB and C/TiO₂. (b) Raman spectra of N-TiO₂@C-CHN, N-TiO₂@C-CTAB, C/TiO₂ and Ti₃C₂ MXene.

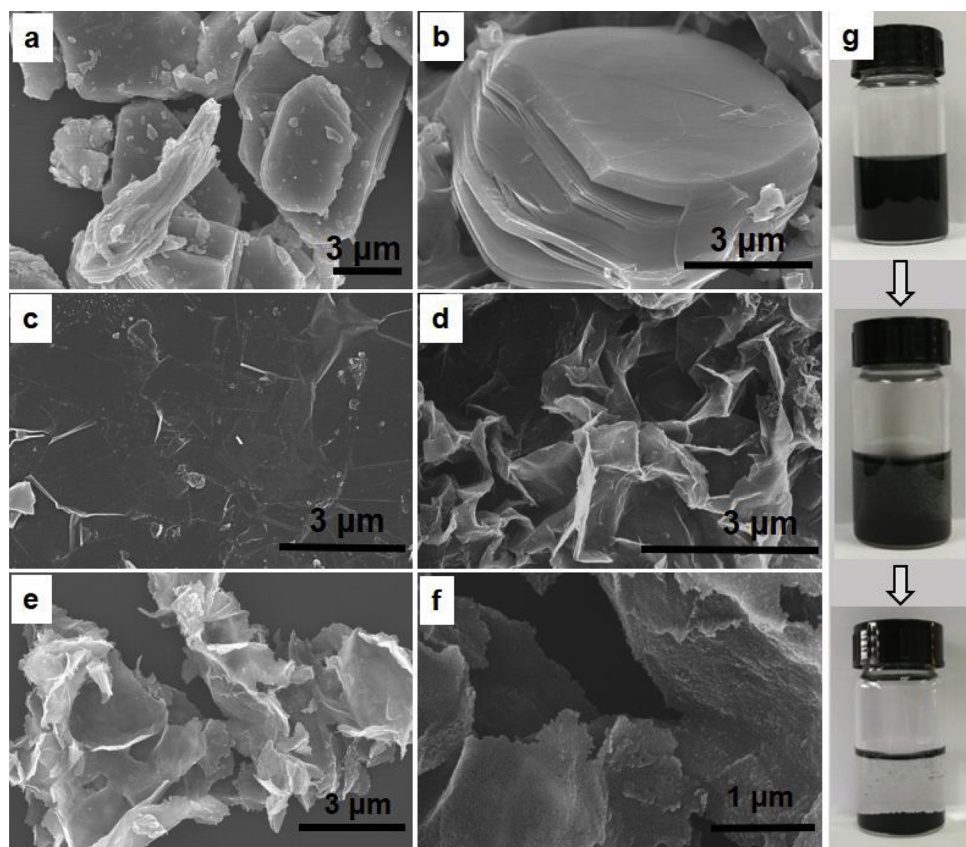


Fig. 2. SEM images of (a) Ti₃AlC₂, (b) multilayer Ti₃C₂ Mxene, (c) ultrathin Ti₃C₂ MXene, (d) electrostatic self-assembled Ti₃C₂ MXene and (e–f) N-TiO₂@C. (g) Optical photographs of electrostatic self-assembly process.

layered structure, and the calcination does not destroy the original framework structure. Obviously, the TiO₂ nanocrystals uniformly distributed on the surface of carbon layer serve as active sites in photocatalytic reaction.

To further clarify the detailed structure of the N-TiO₂@C,

transmission electron microscopy (TEM) measurement was performed. From the TEM images we found that Ti₃C₂ MXene (Fig. 3a) and N-TiO₂@C-CHN (Fig. 3b and c) were both two-dimensional layers with large size, which was in good agreement with their SEM results. Fig. 3c clearly reveals TiO₂ nanocrystals with tens of nanometers in size, and

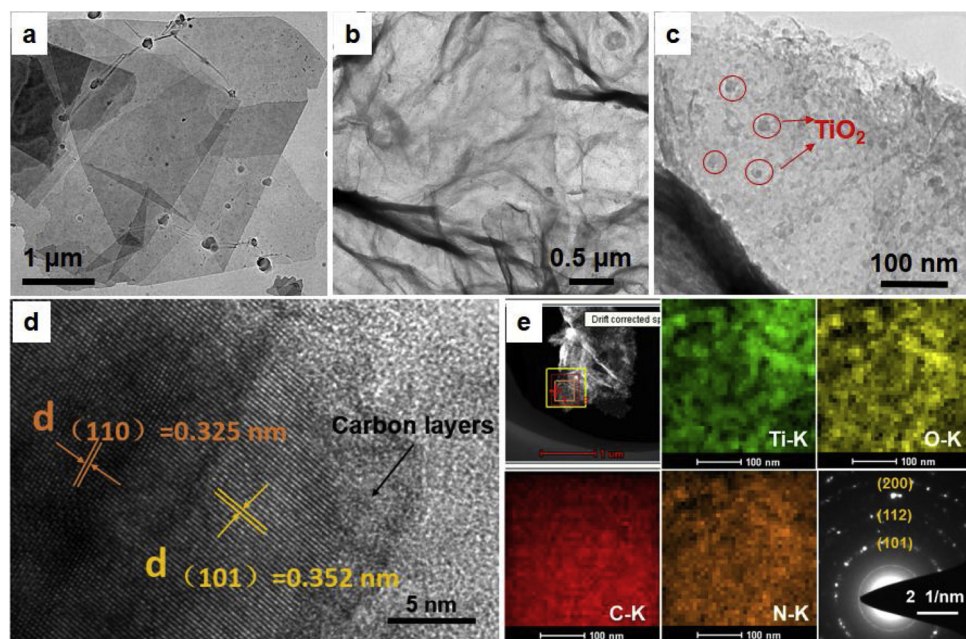


Fig. 3. TEM image of (a) Ti₃C₂ MXene and (b–c) N-TiO₂@C-CHN. HRTEM image of (d) N-TiO₂@C-CHN and (e) STEM image, EDS elemental mapping and SAED pattern of N-TiO₂@C-CHN.

some of the nanocrystals are marked with red circles. Combining with Fig. 2f, it is shown that TiO_2 nanocrystals are distributed on the surface of carbon layer and partly embedded in carbon layer, which indicates that TiO_2 nanocrystals have a strong bonding force with carbon matrix. The high-resolution TEM (HRTEM) image (Fig. 3d) of $\text{N-TiO}_2@\text{C-CHN}$ indicated that the (101) crystal plane of the anatase lattice spacing with 0.352 nm and the (110) crystal plane of the rutile with a lattice spacing of 0.325 nm, which was consistent with its XRD results (Fig. 1a). The STEM image, EDS mapping and SAED of $\text{N-TiO}_2@\text{C-CHN}$ were represented in Fig. 3(e). It could be seen that the four elements C, N, O and Ti were uniformly dispersed on the surface of the sample, which together with EDS (Fig. S1) proved that these elements existed in the catalyst. SAED diffraction was consistent with the anatase lattice spacing. N_2 adsorption-desorption isotherm of $\text{N-TiO}_2@\text{C-CHN}$ (Fig. S2) exhibited a typical type IV adsorption-desorption isotherm with a distinct hysteresis loop at a relative pressure of 0.43–1.0, which indicated that mesopores existed in $\text{N-TiO}_2@\text{C-CHN}$, and the corresponding BJH pore size distribution demonstrated that the pore size is about 12.5 nm.

In order to study the change of chemical bond in the oxidation process of Ti_3C_2 MXene in CO_2 atmosphere, X-ray photoelectron spectroscopy (XPS) was used to characterize elemental composition and valence analysis for $\text{N-TiO}_2@\text{C-CHN}$. The survey spectra of $\text{N-TiO}_2@\text{C-CHN}$

and Ti_3C_2 MXene are shown in Fig. S3. After CO_2 oxidation, the $\text{Ti} 2p_{3/2}$ (455.3 eV) and $\text{Ti} 2p_{1/2}$ (461.2 eV) of Ti_3C_2 MXene (Fig. 4e) were replaced by TiO_2 (Fig. 4a), showing two peaks of $\text{Ti} 2p$ centred at 458.5 and 463.3 eV belong to $\text{Ti} 2p_{3/2}$ and $\text{Ti} 2p_{1/2}$, respectively. The Ti^{3+} sites were studied by electron spin resonance (ESR) spectroscopy (Fig. S4). However, the large, broad signal not detected at $g = 1.98$, indicating that there was no Ti^{3+} site in $\text{N-TiO}_2@\text{C}$ [4,32]. The high-resolution spectra of C 1s (Fig. 4b) displayed four peaks at 284.6, 285.0, 286.1 and 288.7 eV corresponding to C–C, C–N, C–OH and C=O bonds, respectively, indicating that the disappearance of Ti–C band (281.8 eV) of Ti_3C_2 MXene after calcining, as shown in Fig. 4f. In addition, it can be seen from the C 1s spectra (Fig. 4b) that Ti–C bond was not detected around 281.8 eV, illustrating that Ti was not bonded with carbon, and carbon was not doped into the lattice of TiO_2 [4,5,33]. The O 1s XPS spectrum (Fig. 4c) can be split into four peaks centred at 529.5, 529.9, 531.7 and 533.2 eV which belong to O^{2-} , $\text{Ti}=\text{O}-\text{Ti}$, $\text{Ti}-\text{O}-\text{H}$ and $\text{H}-\text{O}-\text{H}$ bonds, respectively. The high-magnification XPS spectrum of N 1s (Fig. 4d) can be divided into three peaks of 398.9, 399.5 and 400.0 eV, which are consistent with N–O, N–Ti–O and N–C bonds respectively. It demonstrate that the N element enters into the TiO_2 lattice in the form of substituting O atom and gets into the carbon matrix in the form of substituting C atom [34,35] and the N element

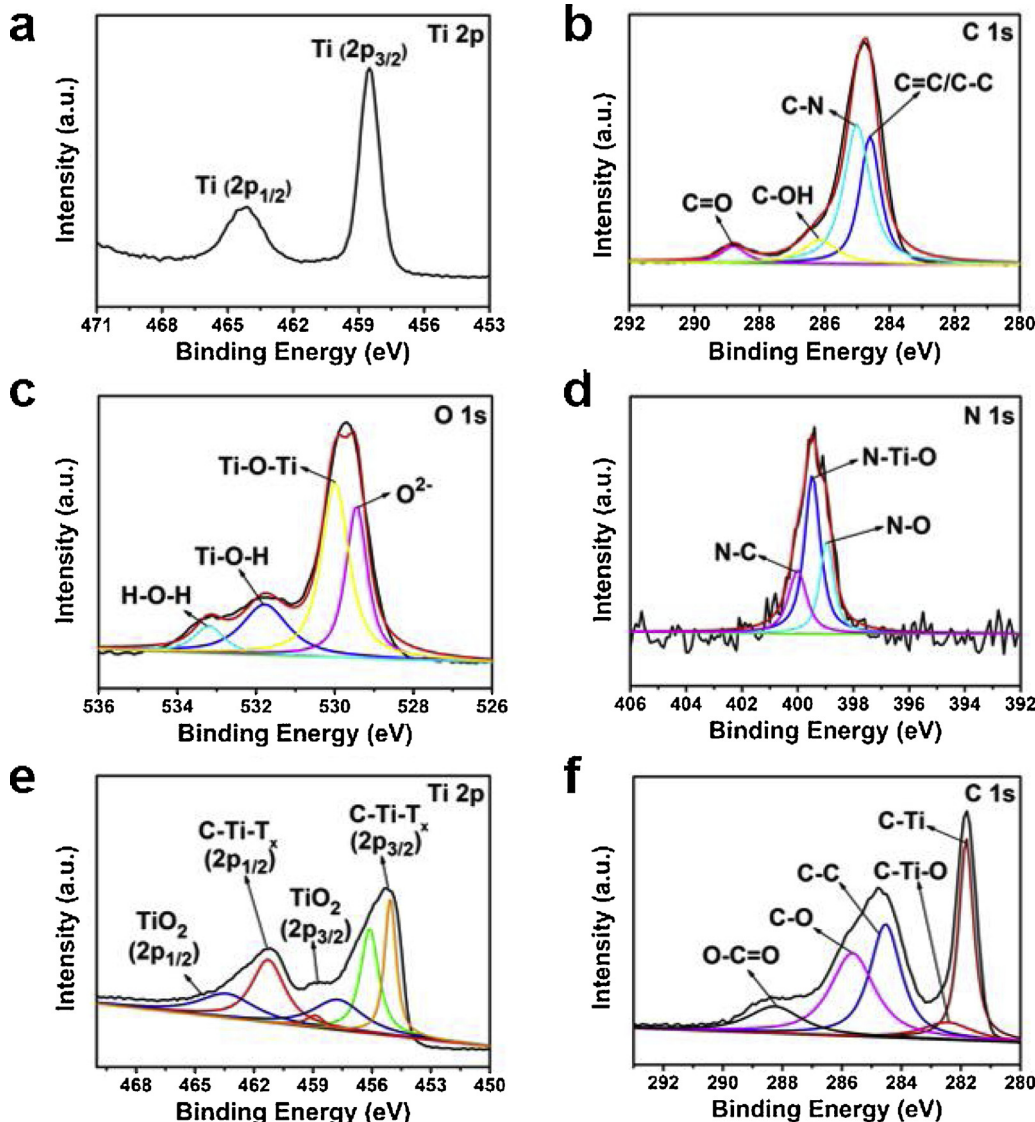


Fig. 4. High-resolution XPS spectra of Ti 2p (a), C 1s (b), O 1s (c) and N 1s (d) of $\text{N-TiO}_2@\text{C-CHN}$. High-resolution XPS spectra of Ti 2p (e) and C 1s (f) of Ti_3C_2 MXene.

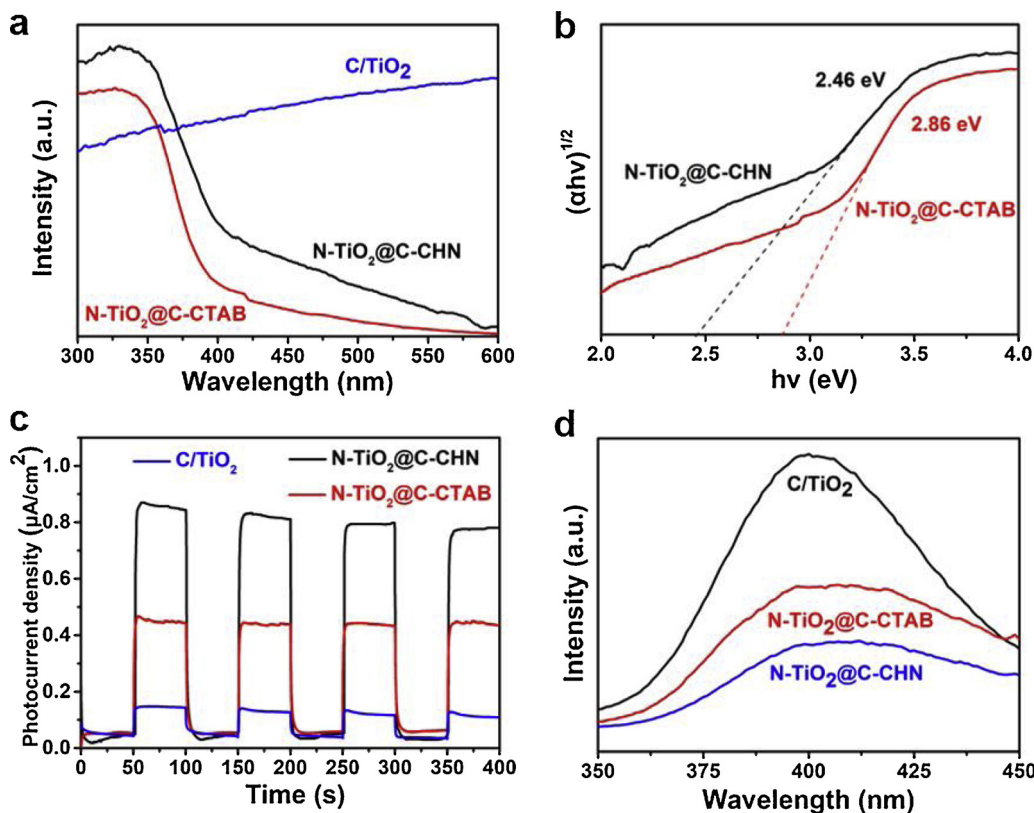


Fig. 5. (a) UV-vis absorption spectra of N-TiO₂@C-CHN, N-TiO₂@C-CTAB and C/TiO₂. (b) The band gap energy of N-TiO₂@C. (c) The photocurrent density curves and (d) photoluminescence spectra of the different samples.

successfully doped into the carbon matrix and TiO₂ nanocrystal. All in all, XPS demonstrated that 2D layered N-TiO₂@C are N-doped TiO₂ nanocrystals supported on N-doped carbon matrix composites.

The optical properties of all samples were investigated in detail. The UV-vis diffuse reflectance spectra of N-TiO₂@C-CHN, N-TiO₂@C-CTAB and C/TiO₂ were shown in Fig. 5a. A flat absorption curve of C/TiO₂ was shown in the UV-vis range [36]. The N-TiO₂@C-CTAB showed an absorption edge at about 405 nm, while N-TiO₂@C-CHN displayed an absorption edge at 435 nm. The absorption of visible light can be attributed to the nitrogen doped into TiO₂ to change the electronic band structure [11]. The bandgaps (Fig. 5b) of N-TiO₂@C-CHN and N-TiO₂@C-CTAB were estimated by the Tauc plot [37], which is derived from the corresponding UV-vis diffuse reflectance spectrum, based on the Eq. (1):

$$\alpha h\nu = A(h\nu - E_g)n \quad (1)$$

where α , ν , h and E_g represent the absorption coefficient, optical frequency, Planck constant and bandgap, respectively, and n corresponds to the transition characteristic in the semiconductor, the value of n is 1 for TiO₂ with direct transition semiconductor properties. Therefore, the band gaps of N-TiO₂@C-CHN and N-TiO₂@C-CTAB are estimated to be about 2.46 eV and 2.86 eV, respectively. The doping of N element into TiO₂ causes the bandgaps of these N-TiO₂@C samples to be smaller than pure TiO₂ semiconductor (3.2 eV) and the light absorption edge red shift, which has been reported in many previous literatures [38–40]. Fig. 5c displays the photocurrent density of photocatalyst cast on ITO as working electrode under visible light irradiation, in which the electrolyte is 0.1 M Na₂SO₄ solution. Compared with C/TiO₂, N-TiO₂@C showed markedly enhanced photocurrent density, and the highest N-TiO₂@C-CHN was about 5.3 times higher than C/TiO₂. Photoluminescence (PL) spectroscopy is an effective tool to reflect the charge separation efficiency and electron transfer ability of photocatalyst, because PL intensity usually derived from the recombination

of photogenerated electrons and holes. Obviously, the PL results of all samples (Fig. 5d) indicate that N-TiO₂@C can transmit photogenerated electrons more efficiently than C/TiO₂, thus reducing the recombination rate of photogenerated carriers. In-situ synthesis of N-TiO₂@C has stronger bonding force, and photogenerated electrons are more easily transported to the two-dimensional carbon layer with nitrogen doping to improve surface functional group [28].

The photocatalytic performance of all samples evaluated by phenol degradation under visible light irradiation ($\lambda > 420$ nm) are demonstrated in Fig. 6a. In general, it is difficult to degrade phenol under visible light using pure TiO₂. Compared with N-TiO₂@C, the hydro-thermally synthesized C/TiO₂ has a phenol degradation rate of only 38.7% within 3 h. The uniformly distributed N-doped TiO₂ nanocrystals in the N-doped two-dimensional carbon matrix, providing a large number of visible light absorption catalytic active sites. N-TiO₂@C-CTAB degrades 81.7% at the same time, and N-TiO₂@C-CHN exhibited the highest degradation rate of phenol of 96% in 3 h. The kinetic behaviors of all samples follow first-order kinetics model, the rate constants of N-TiO₂@C-CHN, N-TiO₂@C-CTAB and C/TiO₂ are calculated to be 1.646×10^{-2} , 0.933×10^{-2} and $0.239 \times 10^{-2} \text{ min}^{-1}$, respectively (Table 1). Fig. S5 displayed the HPLC diagram of phenol degradation by N-TiO₂@C-CHN. The phenol peak (retention time at 4.9 min) weakened with time and a new peak was generated (retention time at 5.75 min), indicating that the phenol was gradually degraded [41]. Cycle stability is another key parameter for a promising catalyst. We further conducted a cyclic production test of N-TiO₂@C-CHN (Fig. 6b), the stability of N-TiO₂@C-CHN is further tested by more reuse cycles are shown in Fig. S6, the photocatalytic degradation efficiency of N-TiO₂@C-CHN is no obvious photocatalytic activity loss after 10 cycles. Fig. S7 demonstrates the XRD pattern, SEM image and Raman spectrum of N-TiO₂@C-CHN after degradation, indicating that the catalyst substantially retains the original crystal form and structure. That is, the N-TiO₂@C catalyst has good stability. The above results

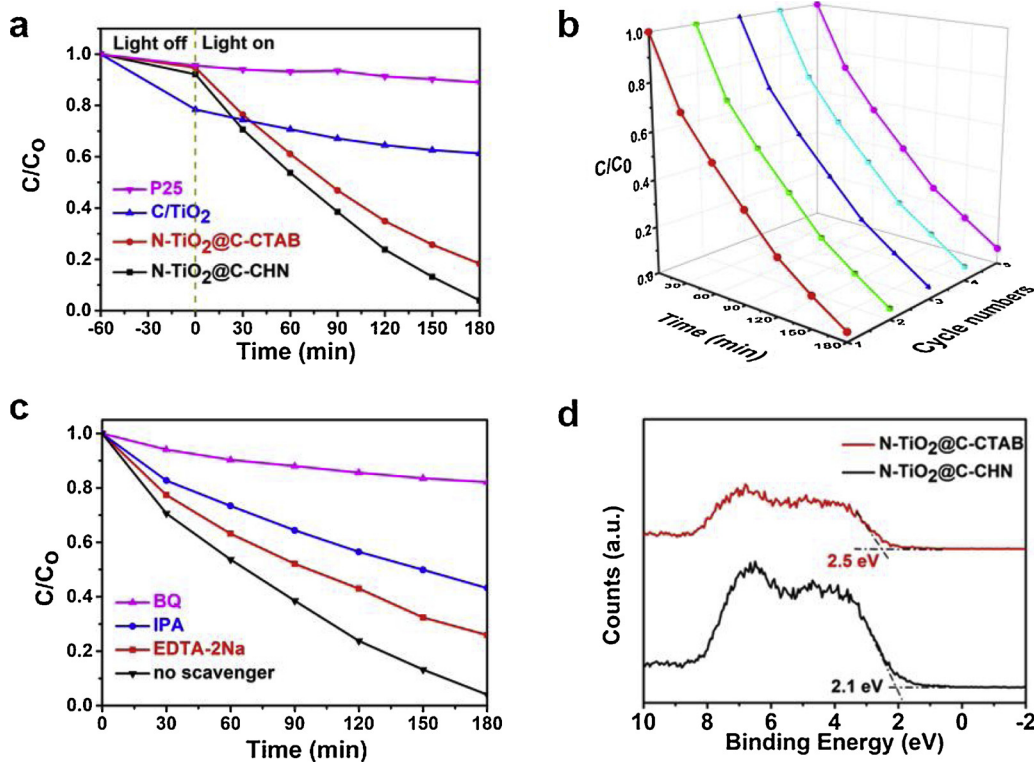


Fig. 6. (a) Phenol degradation curves of N-TiO₂@C-CHN, N-TiO₂@C-CTAB, P25 and C/TiO₂, (b) Recycling performance of N-TiO₂@C-CHN towards phenol degradation, (c) Effects of different reactive species scavengers on the degradation of phenol by N-TiO₂@C-CHN under visible-light illumination, (d) The valence band XPS spectra of N-TiO₂@C.

Table 1
Kinetic constants of N-TiO₂@C-CHN, N-TiO₂@C-CTAB and C/TiO₂ for phenol degradation.

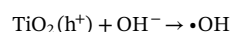
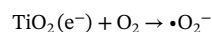
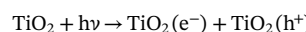
Samples	k (min^{-1})
N-TiO ₂ @C-CHN	1.646×10^{-2}
N-TiO ₂ @C-CTAB	0.933×10^{-2}
C/TiO ₂	0.239×10^{-2}

indicate that the two-dimensional layered nitrogen-doped carbon-supported titanium dioxides derived from Ti₃C₂ MXene by one-step in-situ preparation strategy is a promising composite photocatalyst.

The mechanism of phenol degradation by N-TiO₂@C photocatalyst was elucidated by free radical trapping experiments with p-benzoquinone (BQ, $\cdot\text{O}_2^-$ scavenger), tert-butyl alcohol (IPA, $\cdot\text{OH}$ scavengers) and ethylenediaminetetraacetate (EDTA-2Na, h^+ scavengers). As shown in Fig. 6c, the degradation efficiency of phenol decreased moderately after EDTA-2Na and IPA was added, while the degradation efficiency of phenol decreased significantly after BQ were added. The results reveals that $\cdot\text{O}_2^-$, $\cdot\text{OH}$ and holes are active species in the degradation process. Fig. 6d shows the valence band XPS spectra of N-TiO₂@C. The valence band edge of N-TiO₂@C-CHN and N-TiO₂@C-CTAB are located at 2.1 and 2.5 eV, respectively. Electron spin resonance (ESR) and DMPO (5, 5-dimethyl-1-pyrroline N-oxide) spin trap technology were used to explore the radical species of the catalytic process. Fig. 7a demonstrates DMPO- $\cdot\text{O}_2^-$ radicals. In the dark, there is no ESR signal indicating no superoxide radical production. After visible light illumination, the clear ESR signal of DMPO- $\cdot\text{O}_2^-$ appeared, whereas six peak were generated and were attributed to the reduction of O₂ by photo-generated electrons of N-TiO₂@C. Similarly, Fig. 7b shows DMPO- $\cdot\text{OH}$ radicals. There is no ESR signal in the dark, and a characteristic peak with an intensity ratio of 1:2:2:1 after visible light irradiation indicates the formation of $\cdot\text{OH}$ [42]. Thus, we put forward a possible reaction mechanism as demonstrate in Scheme 2.

Nitrogen doping causes lattice defects, and the N 2p orbitals overlap with the O 2p orbitals, causing the valence band to rise and the TiO₂

band gap to be pulled toward the visible region. Under visible light irradiation, N-doped TiO₂ is excited to generate photogenerated electrons and photogenerated holes, and photogenerated electrons are rapidly transferred to N-doped carbon matrix. The conduction band of the TiO₂ (-0.3 eV) is higher than the conduction band of carbon (-0.08 eV) [43], improved surface functional group carbon as an excellent conductor carbon could quickly catch the photogenerated electrons, thereby improving separation efficiency [29,44,45]. Photogenerated electrons reduce O₂ to produce superoxide radicals (E (O₂/ $\cdot\text{O}_2^-$) = -0.046 V, vs. NHE) [46], photogenerated holes oxidize OH⁻ in water to obtain $\cdot\text{OH}$ radicals (E ($\cdot\text{OH}/\text{OH}^-$) = +1.99 V, vs. NHE). Hydroxyl radicals and superoxide radicals all are active species for phenol degradation, and the corresponding degradation processes is as follows:



4. Conclusion

In summary, a facile strategy is used to prepare highly-stable N-doped TiO₂@C derived from the two-dimensional layered Ti₃C₂ MXene. The nitrogen doping reduces the band gap of TiO₂ nanocrystals and improves its light harvesting from sunlight. And the separation efficiency of photogenerated carriers is significantly improved by the in-situ formation of nitrogen-doped two-dimensional carbon matrix. Consequently, the visible-light catalytic photodegradation of phenol has synergistically and effectively improved with the apparent rate constant k of $1.646 \times 10^{-2} \text{ min}^{-1}$. The N-doped TiO₂@C is a promising photocatalyst for environmental treatment such as wastewater and air purification.

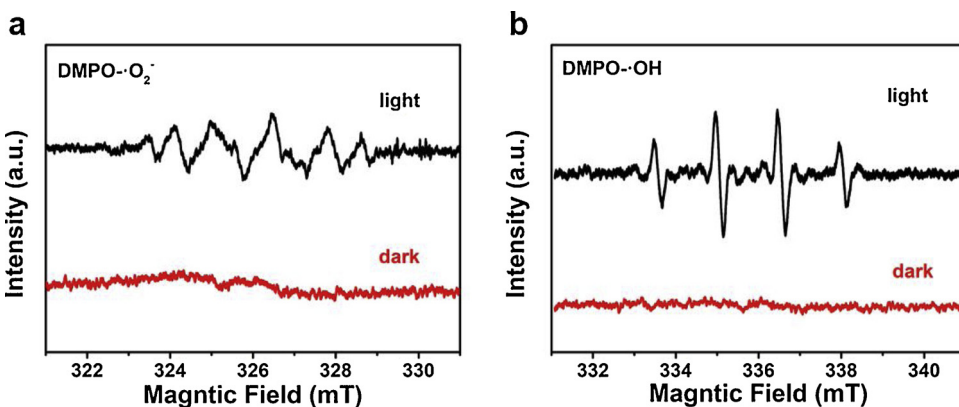
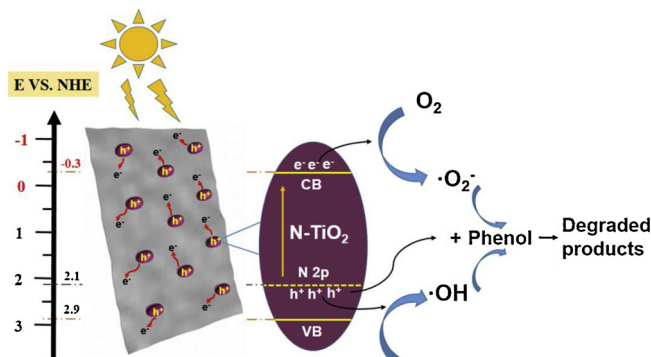


Fig. 7. DMPO spin-trapping ESR spectra of N-TiO₂@C-CHN for (a) ·O₂⁻ in methanol dispersion and for (b) ·OH in water dispersion.



Scheme 2. Schematic diagram of photocatalytic phenol degradation under visible light irradiation with N-TiO₂@C.

Acknowledgements

We gratefully acknowledge the financial support provided by the National Natural Science Foundation of China (51573122, 21722607, 21776190), the Natural Science Foundation of the Jiangsu Higher Education Institutions of China (17KJA430014, 17KJA150009), the National Key Technology R&D Program (2015BAG20B03-06), the Science and Technology Program for Social Development of Jiangsu (BE2015637) and the project supported by the Priority Academic Program Development of Jiangsu Higher Education Institutions (PAPD).

Appendix A. Supplementary data

Supplementary material related to this article can be found, in the online version, at doi:<https://doi.org/10.1016/j.apcatb.2019.03.066>.

References

- [1] T. Hisatomi, J. Kubota, K. Domen, Chem. Soc. Rev. 43 (2014) 7520–7535.
- [2] S. Kumar, L. Devi, J. Phys. Chem. A 115 (2011) 13211–13241.
- [3] B. Cao, G. Li, H. Li, Appl. Catal. B: Environ. 194 (2016) 42–49.
- [4] W. Yuan, L. Cheng, Y. An, et al., Adv. Sci. (2018) 1700870.
- [5] G. Jia, Y. Wang, X. Cui, et al., ACS Sustain. Chem. Eng. 6 (2018) 13480–13486.
- [6] R. Daghbir, P. Drogui, D. Robert, Ind. Eng. Chem. Res. 52 (2013) 3581–3599.
- [7] J. Tian, Z.H. Zhao, A. Kumar, R. Boughton, H. Liu, Chem. Soc. Rev. 43 (2014) 6920–6937.
- [8] L. Shi, C. Xu, D. Jiang, et al., Nanotechnology 30 (2018) 075601.
- [9] H. Sheng, D. Chen, N. Li, Chem. Mater. 29 (2017) 5612–5616.
- [10] Y. Song, N. Li, D. Chen, et al., ACS Sustain. Chem. Eng. 6 (2018) 4000–4007.
- [11] G. Barolo, S. Livraghi, M. Chiesa, J. Phys. Chem. C 116 (2012) 20887–20894.
- [12] G. Yang, J. Zheng, H. Shi, J. Mater. Chem. 20 (2010) 5301–5309.
- [13] Y. Zhang, X. Xiong, Y. Han, et al., Chem. Eng. J. 162 (2010) 1045–1049.
- [14] S. Perera, R. Mariano, K. Vu, N. Nour, O. Seitz, ACS Catal. 2 (2012) 949–956.
- [15] M. Sampayo, R. Marques, P. Tavares, J. Faria, J. Environ. Chem. Eng. 1 (2013) 945–953.
- [16] M. Naguib, M. Kurtoglu, V. Presser, J. Lu, J. Niu, M. Heon, L. Hultman, Adv. Mater. 23 (2011) 4248–4253.
- [17] M. Naguib, V.N. Mochalin, M.W. Barsoum, Y. Gogotsi, Adv. Mater. 26 (2014) 992–1005.
- [18] X. Wu, Z. Wang, M. Yu, et al., Adv. Mater. 29 (2017) 1607017.
- [19] B. Xiao, Y. Li, X. Yu, et al., Sens. Actuators B Chem. 235 (2016) 103–109.
- [20] M. Zhu, Y. Huang, Q. Deng, et al., Adv. Energy Mater. 6 (2016) 1600969.
- [21] Q. Peng, J. Guo, Q. Zhang, et al., J. Am. Chem. Soc. 136 (2014) 4113–4116.
- [22] C. Peng, X. Yang, Y. Li, H. Yu, H. Wang, F. Peng, ACS Appl. Mater. Interfaces 8 (2016) 6051–6060.
- [23] H. Ghassemi, W. Harlow, O. Mashtalir, M. Beidaghi, M.R. Lukatskaya, J. Mater. Chem. A 2 (2014) 14339–14343.
- [24] Z. Li, L. Wang, D. Sun, Y. Zhang, B. Liu, Q. Hu, A. Zhou, Mater. Sci. Eng. B 191 (2015) 33–40.
- [25] O. Mashtalir, K. Cook, V. Mochalin, M. Crowe, M. Barsoum, Y. Gogotsi, J. Mater. Chem. A 2 (2014) 14334–14338.
- [26] Y. Gao, H. Chen, A. Zhou, et al., Nano 10 (2015) 1550064.
- [27] M. Naguib, O. Mashtalir, M.R. Lukatskaya, B. Dyatkin, C. Zhang, V. Presser, Y. Gogotsi, M.W. Barsoum, Chem. Commun. 50 (2014) 7420–7423.
- [28] W. Yuan, L. Cheng, Y. Zhang, H. Wu, S. Lv, L. Chai, X. Guo, L. Zheng, Adv. Mater. Interface 4 (2017) 1700577.
- [29] Q. Liu, L. Ai, J. Jiang, J. Mater. Chem. A 6 (2018) 4102–4110.
- [30] W. Jiang, M. Zhang, J. Wang, et al., Appl. Catal. B: Environ. 160 (2014) 44–50.
- [31] A. Ferrari, D. Basko, Nat. Nanotech. 8 (2013) 235.
- [32] J. Tang, Y. Liu, Y. Hu, et al., Chem. Eur. J. 24 (2018) 4390–4398.
- [33] W. Tu, Y. Zhou, Q. Liu, et al., Adv. Funct. Mater. 23 (2013) 1743–1749.
- [34] J. Wang, W. Zhu, Y. Zhang, et al., J. Phys. Chem. C 111 (2007) 1010–1014.
- [35] X. Yu, Y. Wang, A. Kim, et al., Chem. Phys. Lett. 685 (2017) 282–287.
- [36] J. Low, L. Zhang, T. Tong, et al., J. Catal. 361 (2018) 255–266.
- [37] G. Eperon, S. Stranks, C. Menelaou, et al., Energy Environ. Sci. 7 (2014) 982–988.
- [38] H. Li, Y. Hao, H. Lu, et al., Appl. Surf. Sci. 344 (2015) 112–118.
- [39] C. Han, Y. Wang, Y. Lei, et al., Nano Res. 8 (2015) 1199–1209.
- [40] X. Liu, Z. Xing, Y. Zhang, et al., Appl. Catal. B: Environ. 201 (2017) 119–127.
- [41] T. Cai, L. Wang, Y. Liu, et al., Appl. Catal. B: Environ. 239 (2018) 545–554.
- [42] Y. Huang, P. Wang, Z. Wang, et al., Appl. Catal. B: Environ. 240 (2019) 122–131.
- [43] Y. Wang, J. Yu, W. Xiao, Q. Li, J. Mater. Chem. A 2 (2014) 3847.
- [44] C. Zhang, M. Beidaghi, M. Naguib, et al., Chem. Mater. 28 (2016) 3937.
- [45] N. Yang, Y. Liu, H. Wen, Z. Tang, H. Zhao, Y. Li, D. Wang, ACS Nano 7 (2013) 1504.
- [46] H. Wang, Y. Wu, T. Xiao, et al., Appl. Catal. B: Environ. 233 (2018) 213–225.